Geometry-Preserving Mesh Coarsening of Stochastically Generated Regolith Particles for Use in DEM Simulations

Matthias Weber[1], Phillip Gräfensteiner[1], Tobias Lamping[2], Ralf Ditscherlein[3], Tehya Birch[4], Georg Pöhle[5], Urs A. Peuker[3], Achim O. Seidel[4], Carsten Schilde[2], and Volker Schmidt[1]

September 22, 2026

[1]Institute of Stochastics, Ulm University, Helmholtzstr. 18, 89069 Ulm, Germany
[2]Institute for Particle Technology, TU Braunschweig, Schleinitzstr. 20, 38106 Braunschweig, Germany
[3]Institute for Mechanical Process Engineering and Mineral Processing, TU Bergakademie Freiberg, Agricolastr. 1, 09599 Freiberg, Germany
[4]Airbus Defence and Space, Claude Dornier Str., 88090 Immenstaad, Germany
[5]Fraunhofer Institute for Manufacturing Technology and Advanced Materials IFAM, Winterbergstr. 28, 01277 Dresden, Germany

Abstract

In this paper, a 3D stochastic geometry model for generating artificial regolith particles is proposed. The model is calibrated and validated based on measured X-ray tomographic image data of various regolith simulants. In order to link the resulting database with subsequent numerical DEM simulations, the complexity of particle geometries needs to be controllable. Thus, the proposed model operates in a two-step procedure. First, high-fidelity virtual particles are constructed using a Gaussian random field on the sphere. Second, a mesh coarsening algorithm is applied to limit their geometry to convex polyhedrons with a tunable number of faces. This coarsening algorithm is custom-designed to preserve a selection of key geometric descriptors of the particle geometry. Then, numerical DEM simulations of granular flow are performed using virtually generated particle assemblies to determine key properties of effective bulk behavior, such as the static angle of repose. The quantities are necessary to calibrate the DEM contact parameters so that the simulated flow behavior matches the experimental observations. The results enable a controlled and quantifiable trade-off between structural fidelity and computational complexity, thereby informing future choices of model parameters for large-scale numerical simulations.

Keywords:
Regolith particle, tomographic 3D imaging, stochastic 3D model, mesh coarsening, DEM simulation, regolith flow behavior

1 Introduction

Space exploration is transitioning from short-term missions to sustained surface operations beyond low earth orbit. Current roadmaps envision long-term activities in cislunar space, on the Moon, and eventually on Mars [1]. These ambitions are supported by technological progress and declining launch costs. However, sustainable exploration requires a reduced dependence on terrestrial supply chains.

In-situ resource utilization (ISRU) is a central enabling concept in this context. ISRU aims to extract and process local materials to produce consumables such as oxygen, metals, and construction feedstock [1–3]. On the Moon, the primary accessible resource is lunar regolith, i.e., the unconsolidated material found on the Moon's surface [4]. Oxygen production is of particular interest, as it supports both life support systems and propellant generation, and lunar regolith consists of 40–45% oxygen contained various metal oxides [5]. The ROXY (regolith to oxygen and metals conversion) process, developed by Airbus, uses molten salt electrolysis to extract oxygen and metallic by-products directly from lunar regolith [1, 6, 7]. A miniaturized demonstrator, Mini-ROXY, is currently under preparation for a lunar technology validation mission [8].

The efficiency and reliability of such systems are critically dependent on regolith handling. The regolith must be excavated, transported, stored, and continuously fed into reactors. These operations involve complex granular flow phenomena of highly irregular and angular particles that exhibit a very broad particle size distribution. Under lunar conditions, i.e., reduced gravity, high vacuum, strong thermal gradients, and electrostatic charging, interparticle forces differ significantly from those on Earth. In particular, the very broad particle size distribution introduces additional challenges at both ends of the size spectrum: the finest particles, including submicron fractions, tend to be highly cohesive, whereas coarse particles can promote arching, segregation, and blockage of handling devices. Consequently, cohesive forces and frictional effects may dominate over gravitational loading. As a result, bulk behavior, such as flowability, shear strength, and compressibility, can deviate from terrestrial analogs. Therefore, a predictive understanding of regolith rheology is essential to support the development of ISRU and other applications.

Comprehensive experimental investigations of lunar regolith mechanics under authentic lunar conditions, particularly with reduced gravity, face severe difficulties. A dedicated lunar mission for systematic materials testing would be prohibitively expensive and entail substantial mission risk, especially when probing limits of, e.g., regolith flowability. Ground-based microgravity platforms such as drop towers or parabolic flights require significant quantities of representative lunar material, which is not available. Moreover, such experiments suffer from methodological constraints, including transient high-gravity phases between test intervals and the technical difficulty of simultaneously reproducing vacuum conditions and electrostatic effects.

To mitigate these challenges, terrestrial regolith simulants are often employed, and experimental setups are simplified to replicate selected aspects of the lunar environment. However, regolith simulants differ from genuine lunar regolith in particle morphology, surface texture, and mineralogical composition, and simplified boundary conditions introduce additional uncertainties. The recent availability of high-resolution tomographic image data of the lunar regolith returned by the Apollo [9] and Chang'e-5 missions [10] enables a complementary approach based on computer-assisted image analysis and numerical simulation. Nevertheless, it still makes sense to use terrestrial regolith simulants for this purpose because they are available in much greater variety than the genuine lunar regolith. In the present paper, such a framework will be established based on X-ray micro-computed tomography (micro-CT) measurements of terrestrial regolith samples, which can be subsequently applied to measured image data of actual lunar regolith samples.

In this context, the discrete element method (DEM) plays an important role, which is a well-established numerical technique to simulate the mechanical behavior of granular materials [11, 12]. Note that in the DEM framework each particle is represented as an individual discrete body whose translational and rotational motion is determined by integrating Newton's equations of motion. Interactions between particles are resolved through contact models that account for normal and tangential forces, frictional sliding, rolling resistance, and cohesive effects. Macroscopic bulk behavior emerges from the collective dynamics of many interacting particles. The computational cost of DEM simulations and thus the maximum feasible sample size strongly depends on particle shape complexity. In particular, large numbers of highly non-convex particles render contact detection and force evaluation computationally expensive. Consequently, particles are typically approximated by simplified, often convex geometries, while unresolved features, such as surface roughness, are implicitly incorporated through calibrated contact parameters, such as static and dynamic friction and cohesion [13, 14].

In DEM simulations, various approaches are used to represent the shape of particles. These include composite particles such as multi-sphere models, particles with combined surfaces such as polyhedra, spherocylinders, or cylinders, smooth and continuous surface particles such as ellipsoids, superquadrics, or pseudo-potential particles, as well as discretized particles [15, 16]. For the present study, non-spherical particles based on polyhedra are used. The original formulation of the contact laws for polyhedra goes back to Cundall [17, 18] and has since been extended in several subsequent studies. In representing particles, it is important to strike a suitable balance between geometric accuracy and computational cost. Since polyhedral particles are mesh-based, this trade-off is governed primarily by the number of faces: increasing the number of faces improves the geometric representation but also increases the computational effort significantly. Therefore, suitable procedures are required to derive low-resolution polyhedra from high-fidelity particle geometries to balance accuracy and efficiency [19].

In the present paper, we propose a stochastic geometry model [20] for granular materials, with a particular focus on regolith particles, that systematically addresses this trade-off between accuracy and cost. The model is capable of generating low-poly mesh representations with an arbitrary number of faces while preserving user-defined target properties. In a first step, a high-fidelity model is fitted to three-dimensional particle geometries obtained from micro-CT measurements. The virtual particles drawn from this model are statistically consistent with the measured ensemble. In a second step, a tunable mesh coarsening procedure based on simulated-annealing optimization [21] generates low-poly meshes with a prescribed number of faces. The objective function can be formulated to preserve selected geometric descriptors, such as particle volume, aspect ratio, or surface area, thereby ensuring a controlled approximation of the original shape. As the resulting low-poly meshes are directly compatible with DEM simulations, the proposed framework enables, first, a systematic investigation of how mesh resolution influences simulation outcomes and which geometric descriptors must be preserved for reliable predictions, and second, virtual materials testing of regolith under lunar conditions.

This work contributes to the development of the UPREB (universal predictors of regolith rheology and behavior) framework, which aims to establish a predictive model for regolith behavior in static and dynamic situations [22]. This provides a pathway toward numerically assessing regolith handling, transport, and processing strategies without the need for extensive physical testing under lunar conditions.

The remainder of this paper is organized as follows. In Section 2, we introduce the investigated regolith simulants and their three-dimensional X-ray micro-CT measurements, define the geometric descriptors used to characterize individual particles, and describe the high-fidelity shape modeling and tunable mesh coarsening methodology. In Section 3, we present the model calibration, evaluate the quality of the statistical fit, and assess the performance and flexibility of the mesh coarsening approach. Finally, we discuss the implications of our findings and outline how the proposed framework can be applied to investigate regolith behavior under lunar conditions. Section 4 concludes.

2 Materials and methods

In the following, we introduce the materials and methods used throughout this manuscript. This includes a description of the measured image data of regolith simulants, particle descriptors and tools for stochastic 3D modeling.

2.1 Regolith simulants

For the development of the proposed stochastic 3D model, we consider measured image data from seven regolith simulants discussed in [23]. These comprise four mare simulants (JSC-1A, LMS-1, OPRL2N, CSM-LMT-1) and three highland types (CSM-LHT-1, OB1A, LHS-1). These regolith simulants were characterized by X-ray micro-CT measurements. The workflow comprises particle-discrete sample preparation, tomographic imaging, and data processing with subsequent segmentation.

To enable particle-wise analysis, we applied the following sample preparation protocol [24]. The regolith particles were thoroughly mixed with carbon black and then embedded in epoxy resin. The nanometer scale carbon black effectively coated individual particles and thereby prevented agglomeration. As carbon black and epoxy resin similarly attenuate X-rays, processing of the collected image data and segmentation were thus facilitated.

Three-dimensional imaging was performed on 2 mm diameter samples using laboratory-based X-ray micro-CT on a Xradia 510 VERSA by ZEISS, Germany, with acceleration voltage: 80 keV, beam power: 7 W, exposure time: 1.5 s, binning: 2, filter: Zeiss standard LE4 and a voxel resolution of approximately 2.3 µm. During measurement, the sample was rotated relative to a fixed detector to acquire a series of projection images that were reconstructed into volumetric datasets using standard filtered back projection algorithms. All regolith simulants were measured under identical scanning conditions to ensure comparability.

For particle-wise analysis, volumetric data was processed using a supervised two-step segmentation workflow implemented in Ilastik [25]. First, a pixel classifier was trained to distinguish material from background. Subsequently, an automated object-classification routine identified and labeled individual particles throughout the 3D dataset.

The resulting data, which will be used for fitting and validating the model, is present as triangular meshes of measured particles. This limits the influence of discretization errors on subsequent operations and allows for easy calculation of various geometric descriptors for each particle. Similarly, we will use triangular meshes for particles drawn from the stochastic geometry model presented in this paper. For more details on materials, sample preparation, and image acquisition, see [23].

2.2 Geometric descriptors

The mechanical behavior and rheology of granular materials originate from two main sources. First, intermolecular and electrostatic forces govern adhesion and, particularly for fine particles, can dominate the overall contact response. Second, geometric features operate on multiple length scales. These range from submicron surface roughness to larger-scale shape features that govern mechanical interlocking.

In the context of DEM simulations, submicron roughness and spatial variations in surface chemistry cannot be resolved explicitly due to limited geometric resolution and the corresponding computational effort. Their effects must therefore be incorporated implicitly through calibrated contact parameters. Accordingly, the stochastic geometry model for particle shapes developed in this paper focuses on reproducing those geometric features that are observable via X-ray micro-CT.

The following geometric descriptors are used to characterize particle morphology, where the **particle volume**, denoted by $V > 0$, represents the most fundamental geometric descriptor. It is often useful to express this quantity using the volume-equivalent radius, i.e., the radius of a sphere with the same volume. The **surface area**, denoted by $A > 0$, serves as a complementary descriptor to the volume, capturing the extent of the particle boundary. The **sphericity**, denoted by $S \in [0, 1]$, quantifies the degree to which a particle approaches a spherical shape by using the ratio of the surface area of a volume-equivalent sphere to the surface area of the particle [26]. For a particle with volume V and surface area A, it is formally given by

$$S = \frac{\pi^{1/3}(6V)^{2/3}}{3A}, \tag{1}$$

where $S = 1$ if the particle is perfectly spherical and $0 < S < 1$ otherwise. The **minimum diameter** $D_{\mathrm{min}} > 0$ and the **maximum diameter** $D_{\mathrm{max}} > 0$ are the shortest and longest edges, respectively, of the (oriented minimum-volume) cubic bounding box that completely contains the particle. The **aspect ratio** of a particle, denoted by $AR > 1$, is defined by

$$AR = \frac{D_{\max}}{D_{\min}}, \tag{2}$$

providing a measure of the elongation of the particle. Finally, the **convex hull volume**, denoted by $CH > 0$, is defined as the volume of the convex hull of the particle.

The descriptors stated above are computed from voxelized image data using the python package `trimesh` [27].

2.3 Stochastic particle model

In order to generate virtual regolith simulant particles from the stochastic 3D model considered in this paper, we first identify each particle observed in the tomographic image data with a so-called radius function $r\colon [0,\pi] \times [0, 2\pi) \to (0, \infty)$, which encodes the distance from a pre-defined point to the boundary along the direction given by the pair of angles $(\theta, \phi) \in [0,\pi] \times [0, 2\pi)$. This identification requires the particles to be star-shaped, i.e., there exists a so-called star-point within each particle from which all straight lines to the boundary are completely contained within the particle. Under this mild assumption, the distance to the boundary from the star-point along a given direction is unique, and the corresponding radius function is well defined.

Any such radius function can be expressed using a series expansion of the form

$$r = \sum_{l=0}^{\infty} \sum_{m=-l}^{l} c_{l,m} Y_{l,m}, \tag{3}$$

where $Y_{l,m}\colon [0,\pi] \times [0, 2\pi) \to \mathbb{R}$ are the (real) spherical harmonics functions with degree $l \in \mathbb{N}_0 = \{0, 1, 2, \ldots\}$ and order $m \in \{-l, \ldots, l\}$, and $c_{l,m} \in \mathbb{R}$ are the so-called spherical harmonics coefficients of r. Note that the outer sum considered in Eq. (3) can be cut at an arbitrary degree $l_{\max} \in \mathbb{N}_0$ to obtain a numerically tractable approximation of the original function r. Thus, for any particle $P \subset \mathbb{R}^3$ that fulfills the assumptions mentioned above, instead of the spherical harmonics representation given in Eq. (3) we consider the approximate representation

$$\widehat{P}_{l_{\max}} = \sum_{l=0}^{l_{\max}} \sum_{m=-l}^{l} c_{l,m} Y_{l,m}, \tag{4}$$

see [28, 29] for more information on spherical harmonics functions.

In order to generate a new (random) virtual particle using this representation, we draw a (random) set of spherical harmonics coefficients $c_{l,m} \in \mathbb{R}$. More precisely, we model these coefficients using independent Gaussian random variables, where $c_{0,0}$ and $c_{l,m}$ are $\mathcal{N}(\mu, A_0)$ and $\mathcal{N}(0, A_l)$ distributed, respectively, for any $l \in \mathbb{N} = \{1, 2, \ldots\}$ and $m \in \{-l, \ldots, l\}$. Here, $\mathcal{N}(\mu, \sigma^2)$ denotes the Gaussian distribution with mean μ and variance σ^2, and $(A_l)_{l\in\mathbb{N}}$ is the so-called angular power spectrum. Under these modeling assumptions for the spherical harmonics coefficients, the resulting radius function defined by Eq. (3) is an isotropic Gaussian random field on the sphere [30, 31], whose distribution is uniquely defined by the value of μ and the angular-power spectrum $(A_l)_{l\in\mathbb{N}}$, which can easily be estimated from image data after determining the spherical harmonics coefficients of every measured particle. The python package `pyshtools` [32] was used to convert between triangular mesh and spherical harmonics representations.

2.4 Mesh simplification

The computational costs of DEM simulations are heavily influenced by the complexity of the particle shapes. Triangular mesh representations of particles, such as those generated by the proposed spherical harmonics model, are typically non-convex and, at standard mesh resolutions, can be prohibitively complex for use in DEM simulations. To address this challenge, we enhance the model with a custom mesh simplification method that produces convex polyhedrons with a selectable number of facets. This method is designed to strike a balance between geometric fidelity and computational feasibility. Moreover, depending on the specific application, certain aspects of particle geometry are known to have a greater impact on mechanical behavior than others [33, 34]. Therefore, a mesh simplification method suitable for DEM simulation should be able to preserve a desired selection of key geometric descriptors. Existing mesh simplification techniques, such as those based on quadric error metrics [35], variational shape approximation [36] or mesh decimation [37] maintain the visual quality of the meshes but do not directly preserve specific geometric descriptors of the original mesh, such as aspect ratio or surface area of particles.

To address these limitations, we propose an optimization-based approach. In this procedure, we consider a particle to be defined by an arbitrary mesh $M \subset \mathbb{R}^3$, which we identify with the three-dimensional volume that it encloses. The original mesh M is then approximated by a convex polyhedron $\widehat{M} \subset \mathbb{R}^3$ with n facets for some integer $n > 4$. Formally, $\widehat{M}$ can be written as the intersection of n half-spaces $H_1, \dots, H_n \subset \mathbb{R}^3$, i.e.,

$$\widehat{M} = \bigcap_{i=1}^{n} H_i. \tag{5}$$

For each $i \in \{1, \dots, n\}$, the half-space H_i is one of the parts that results from the splitting of the three-dimensional space into two parts by a plane. It can be characterized by a vector $p_i \in \mathbb{R}^3 \setminus \{0\}$ whose direction is normal to the splitting plane and whose length is equal to the offset of the plane with respect to the origin. Formally,

$$H_i = \left\{ x \in \mathbb{R}^3 \colon \left\langle x, \frac{p_i}{|p_i|} \right\rangle \leq |p_i| \right\}, \tag{6}$$

where $|p_i| \in \mathbb{R}$ denotes the Euclidean norm of p_i and $\langle x, y \rangle$ is the inner product of $x, y \in \mathbb{R}^3$. Thus, any set of n non-collinear points $p_1, \dots, p_n \in \mathbb{R}^3 \setminus \{0\}$ defines a convex polyhedron through Eqs. (5) and (6), which will be denoted by $\widehat{M}(p_1, \dots, p_n)$.

The optimization procedure iteratively perturbs the points $p_1, \dots, p_n$ using a simulated-annealing-based approach [21] to minimize a given loss function. To maintain flexibility with respect to the desired geometric descriptors that should be retained, we consider a general loss function that is given as a linear combination of various individual metrics. One of these metrics is the intersection-over-union (IoU) between $\widehat{M}(p_1, \dots, p_n)$ and the original mesh M, i.e.,

$$\mathrm{IoU}(M, \widehat{M}) = 1 - \frac{V(M \cap \widehat{M})}{V(M \cup \widehat{M})} \in [0, 1], \tag{7}$$

where $V(\cdot)$ denotes volume, and $\cap$ and $\cup$ represent the intersection and union of two meshes, respectively. Typically, the IoU is defined only by the ration on the right-hand-side of Eq. (7). However, for our usage in a minimization problem it is convenient to define the IoU such that the value of $\mathrm{IoU}(M, \widehat{M})$ is equal to 0 if M and $\widehat{M}$ coincide and equal to 1 if they are disjoint.

Additional elements of the loss function may include the relative error of specific geometric descriptors. If $D \in \mathcal{D}$ is any descriptor from the set of descriptors $\mathcal{D} = \{V, S, D_{\min}, D_{\max}, AR, CH\}$ introduced in Section 2.2, then the relative error ε_D related to that descriptor is given by

$$\varepsilon_{\mathrm{D}}(M, \widehat{M}) = \frac{|\mathrm{D}(M) - \mathrm{D}(\widehat{M})|}{\mathrm{D}(M)}, \tag{8}$$

where $\mathrm{D}(\cdot)$ denotes the value of the given descriptor as defined in Section 2.2. From these quantities, we can construct the loss function

$$L(M, \widehat{M}) = \alpha_{\mathrm{IoU}} \mathrm{IoU}(M, \widehat{M}) + \sum_{D \in \mathcal{D}} \alpha_{\mathrm{D}} \varepsilon_{\mathrm{D}}(M, \widehat{M}), \tag{9}$$

where $\alpha_{\mathrm{IoU}} \in \mathbb{R}$ and $\alpha_{\mathrm{D}} \in \mathbb{R}$ for each $D \in \mathcal{D}$ are given weights.

To obtain an initial set of points $p_1, \ldots, p_n \in \mathbb{R}^3$ for the optimization procedure, we compute the convex hull of the original mesh M and apply fast quadric mesh simplification [35, 38] as implemented in the python package `trimesh` [27]. We define a maximum number of iterations $k_{\max} = 100$ and a monotonically decreasing temperature function $T \colon \{1, \ldots, k_{\max}\} \to (0, 1]$, $k \mapsto T_0 \gamma^k$, where $T_0 = 0.2$ and $\gamma = 0.9$. The optimization then proceeds iteratively for each $k = 1, \ldots, k_{\max}$ as follows.

1. Compute $L = L\big(M, \widehat{M}(p_1, \ldots, p_n)\big)$
2. Randomly select $i \in \{1, \ldots, n\}$
3. Sample p_i' from $\mathcal{N}(p_i, \sigma)$, where $\sigma = \frac{1}{n} \sum_{i=1}^{n} |p_i|$
4. Compute $L' = L\big(M, \widehat{M}(p_1, \ldots, p_{i-1}, p_i', p_{i+1}, \ldots, p_n)\big)$
5. If $L' < L$, update $p_i = p_i'$
6. Else, update $p_i = p_i'$ with probability $T(k)$

Note that perturbations that temporarily worsen the loss are allowed with a small, continuously decreasing probability. This important feature of the simulated-annealing method helps to escape local minima, thus improving the long-term performance of the algorithm [21].

2.5 Data Handling

For practical usage and, in particular, large-scale DEM simulations of bulk behavior, a data handling strategy is needed to store generated particles alongside with relevant metadata. While the particle geometries generated from the stochastic geometry model and mesh coarsening method discussed above are suitable for use in DEM simulations, practical workflows using software such as ANSYS Rocky, may benefit from further improvements.

In particular, the number of distinct particle geometries used within a DEM simulation is related to memory usage and computational cost. Thus, computation may be facilitated by limiting the number of distinct geometries by constructing a dataset based on a finite set of representative particle shapes, along with their corresponding weights and size distributions. Representative particles may be considered to capture the characteristic geometric features of a subset of the whole sample.

Formally, each dataset consists of N representative particles $P_1, \ldots, P_N \subset \mathbb{R}^3$ for some $N \in \mathbb{N}$, where each particle is given as a triangular mesh and normalized to unit volume. For each $i \in \{1, \ldots, N\}$, the representative particle P_i is equipped with a distribution function $F_i \colon \mathbb{R} \to [0, 1]$ of particle size and a corresponding weight α_i, where $\alpha_i \geq 0$ and $\sum_{i=1}^{N} \alpha_i = 1$. For DEM simulations, individual particles are then generated by sampling a particle class $i = 1, \ldots, N$ according to weights α_i, drawing a size from the corresponding distribution function F_i, and scaling the representative particle P_i accordingly.

For storage of such particle datasets, we define a structured database format. Meshes, i.e., geometries that can be used as representative particles, are stored as individual STL files. For each dataset, a JSON file is created that contains references to the appropriate STL files of representative particles, their associated size distributions, and class weights. Moreover, the dataset contains metadata such as model parameters (maximum spherical harmonics degree, angular power spectrum, coarsening settings, etc.) and information on the underlying experimental data and processing steps. This standardized format enables reproducibility and facilitates systematic parameter studies.

Using the ANSYS Rocky python scripting interface, we can automatically import the meshes and parameters of a given dataset into a DEM simulation. Similarly, the results obtained from DEM simulations, such as the angle of repose, are stored as JSON files in the same database structure and reference the underlying particle dataset, simulation parameters, and further metadata. This data management approach provides a link between particle generation, simulation, and analysis, allowing systematic investigation of microstructure–property relationships for regolith systems.

2.6 DEM simulation of static angle of repose

To evaluate the suitability of the generated particle geometries for DEM simulations, the static angle of repose is simulated using the methodology described in [13, 14]. Here, the static angle of repose of a granular material is defined as the steepest slope of an unconfined pile of that material that remains stable and does not flow or collapse. It is sensitive to particle shape and size, as well as contact mechanics, thereby linking the geometric particle model described in the previous sections to the effective properties of bulk material. The input particles for the DEM simulations are obtained from the previously defined database as a set of representative particles, corresponding size distributions, and weights. A large number of individual particles are generated from the representative particles as described above. To improve computational efficiency, a coarse-graining with a factor of 10 was employed, which is a common method used in DEM simulations to reduce computational cost [39] by enlarging all particle sizes (see particle sizes in Table 1) by a given factor.

The simulations are performed using ANSYS Rocky. Interparticle interactions are modeled using the Hertz contact law [40] in the normal direction from the particle density, particle Young's modulus and coefficient of restitution. The tangential direction is described via the Mindlin-Deresiewicz model [41] from the coefficients of static and dynamic friction and Poisson's ratio. In addition, cohesive effects are taken into account using the Johnson–Kendall–Roberts (JKR) model [42] with a corresponding surface energy. The contact parameters are summarized in Table 1. In addition, the geometric data used for the simulation of the static angle of repose are listed in Table 2.

Table 1: Parameter values used in the DEM simulations.

Parameter	**Value**
Particle density [$\mathrm{g\,cm^{-3}}$]	3.075
Particle Young's modulus [GPa]	30
Poisson's ratio [-]	0.2
Static friction coefficient [-]	0.8
Dynamic friction coefficient [-]	0.8
Surface energy [$\mathrm{mJ\,m^{-2}}$]	10
Number of different particle geometries [-]	10
Particle sizes [µm]	25, 37, 56, 84, 125
Number of faces for each particle [-]	20
Coarse-graining factor [-]	10

Table 2: Geometric data for the simulation of the static angle of repose.

Parameter	**Value**
Cylinder diameter [cm]	2
Cylinder height [cm]	8
Fill height [cm]	2.5-3
Number of particles [-]	378,000
Total particle mass [g]	15

The angle of repose is determined by a lifting cylinder test. For this, a desired volume of particles is packed into a cylinder of a given diameter and left to settle under gravity. The cylinder is then vertically removed at a constant speed, leading to the collapse of the material and the formation of a conical pile. When the pile has settled, the slope of the pile is measured to determine the static angle of repose. This provides a quantitative measure of the bulk flow behavior. The measured static angle of repose can then be used for DEM calibration, in which contact parameters such as the friction coefficient and cohesion are adjusted so that the flow behavior of the simulated powder matches the one observed in experiments that apply the same measurement procedure. The process is visualized in Figure 1. The particles visible on the surface of the blue bottom plate in Figure 1 are stuck to the plate due to the high cohesiveness of the powder.

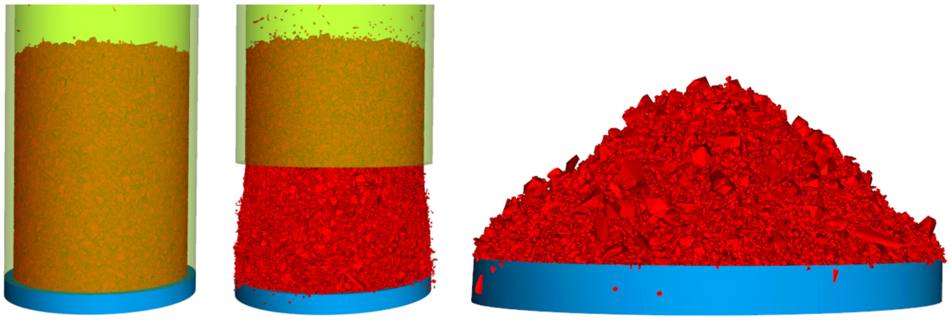

Figure 1: DEM Simulation procedure for the static angle of repose at different simulation times. The right-most image has been enlarged for visual clarity.

3 Results and discussion

3.1 Spherical harmonics model

We fit the spherical harmonics model introduced in Section 2.3 to the measured particles of the seven different regolith simulants stated in Section 2.1. For this, we need to choose a suitable value for the maximum degree $l_{\max}$ at which the series representation, given in Eq. (3) is cut. The choice of $l_{\max}$ balances complexity and fidelity of the resulting fit as illustrated in Figure 2.

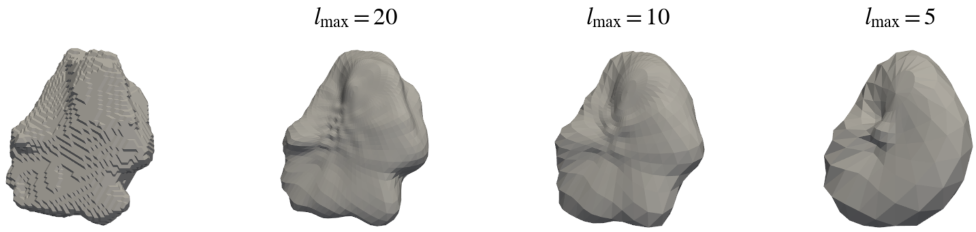

Figure 2: Measured particle of CSM-LHT-1 (left) and spherical harmonics expansions with different degree $l_{\max}$ fitted to the same particle.

In order to quantitatively analyze the goodness-of-fit for varying values of $l_{\max}$, we determine the descriptors introduced in Section 2.2 based on measured particles and the corresponding spherical harmonics approximations, respectively, with varying maximum degrees $l_{\max}$ for the particles of every simulant group. We then determine the root mean squared relative error (RMSRE) defined by

$$\mathrm{RMSRE} = \sqrt{\frac{1}{m}\sum_{i=1}^{m}\left(\frac{D(P_i) - D(\widehat{P}_{i,l_{\max}})}{D(P_i)}\right)^2}, \tag{10}$$

where $m \in \mathbb{N}$ is the number of particles within the considered simulant group, $D \in \mathcal{D}$ is any descriptor from the set of descriptors $\mathcal{D} = \{V, S, D_{\min}, D_{\max}, AR, CH\}$ introduced in Section 2.2, and $\widehat{P}_{i,l_{\max}}$ is the spherical harmonic approximation of the i-th particle P_i, truncated at degree $l_{\max}$, as defined in Eq. (4). The results obtained in this way are visualized in Figure 3. Although volume is a descriptor that is approximated more and more accurately with increasing values of $l_{\max}$, the RMSRE values of the remaining descriptors appear to be stabilizing around $l_{\max} = 10$, which indicates that truncating the outer sum in Eq. (4) at $l_{\max} = 10$ is a reasonable middle-ground between complexity and accuracy.

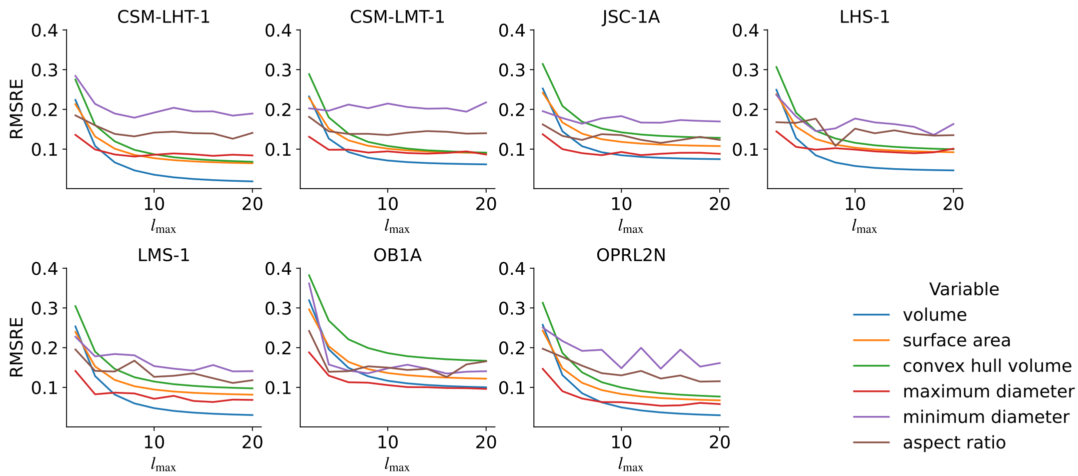

Figure 3: Root mean squared relative errors of the geometric descriptors for spherical harmonics representations of measured particles of the seven simulants and for different values of the maximum degree $l_{\max}$.

After choosing the value of $l_{\max} = 10$, we can now draw new realizations from the particle model described in Section 2.3. In the following, we discuss the goodness-of-fit of these virtually generated particles for the chosen sample population of CSM-LHT-1 in more detail. We use the volume-equivalent radius to represent the particle volumes, as the cubic scaling of the volume introduces a large range in the data that prevents a direct comparison on a common axis.

In particular, Figure 4 shows number-weighted histograms of the volume-equivalent radius, the surface area and the aspect ratio for measured particles from the CSM-LHT-1 sample and particles drawn from the fitted spherical harmonics model.

The fit of the volume-equivalent radius shows a good agreement for most of the radii, with a slight shift towards increased values for the model. The histogram of the CSM-LHT-1 sample shows additional minor peaks for higher radii above 15, while all virtually generated particles have volume-equivalent radii below 22. These larger particles affect the estimation of the mean particle size in the stochastic particle model, which causes the overall shift towards larger particle radii compared to the majority of particles in the CSM-LHT-1 samples within the range of 0–15. The surface area behaves similar, although the influence of larger particles is more pronounced in the histogram due to the quadratic scaling of the surface area. The differences between the data and the model with respect to the aspect ratio is in line with the higher values of the RMSRE for the aspect ratios

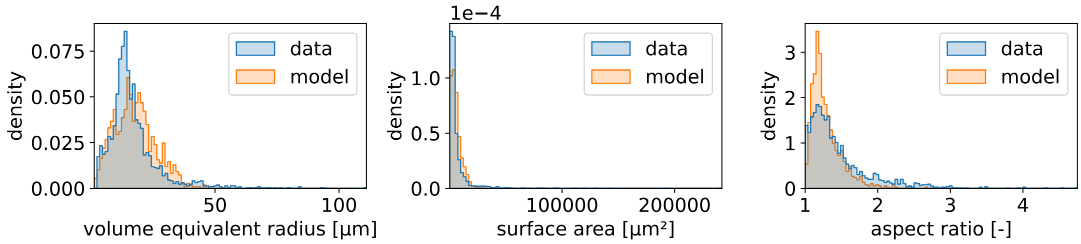

Figure 4: Univariate (number-weighted) probability densities of geometric descriptors for measured particles and particles simulated from the spherical harmonics model for the CSM-LHT-1 sample. Depicted are the volume (left), the surface area (center) and the aspect ratio (right).

of the CSM-LHT-1 sample shown in Figure 3.

The discrepancies with respect to volume equivalent radius become more pronounced when considering volume-weighted histograms, as shown in Figure 5. Large particles that appear only rarely in a number-weighted sense cannot be properly reproduced by a model consisting of a single Gaussian random field as described above. Even though only a small number of these large particles exist in the data, they contribute a major part in a volume-weighted sense. However, the stochastic model generates individual particles according to a number-weighted distribution. To capture these effects, the model could be extended by considering a mixture of Gaussian random fields, which enables reproducing multi-modal volume distributions and varying correlations with particle shape for different size classes, thereby also improving the fit of shape descriptors such as the aspect ratio.

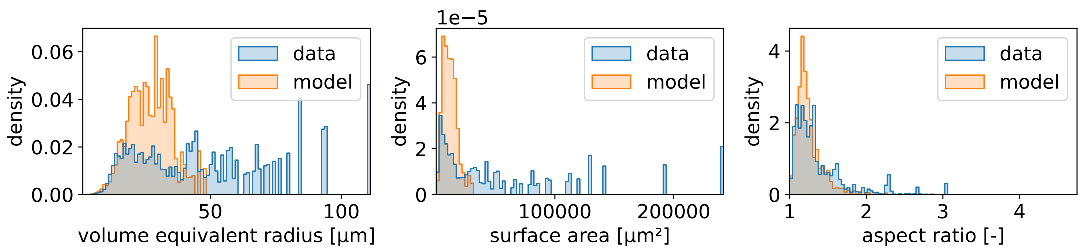

Figure 5: Univariate (volume-weighted) histograms of geometric descriptors for measured particles and particles simulated from the spherical harmonics model for the CSM-LHT-1 sample. Depicted are the volume (left), the surface area (center) and the aspect ratio (right).

Figure 6 illustrates the (number-weighted) bivariate probability densities of descriptor pairs for measured and simulated particles. The general shape of the bivariate densities matches well between measured and simulated data. In particular, the correlation between the univariate descriptors is reproduced accurately. This is an important observation, as capturing solely the univariate distribution of geometric descriptors without considering their joint multivariate distributions may not be enough to capture granular flow behavior of irregularly shaped particle systems [43]. The main discrepancies here are due to the differences in the univariate distribution of aspect ratios. Additionally, we observe a slightly higher variance of surface areas for any given volume in the measured image data compared to the model realizations.

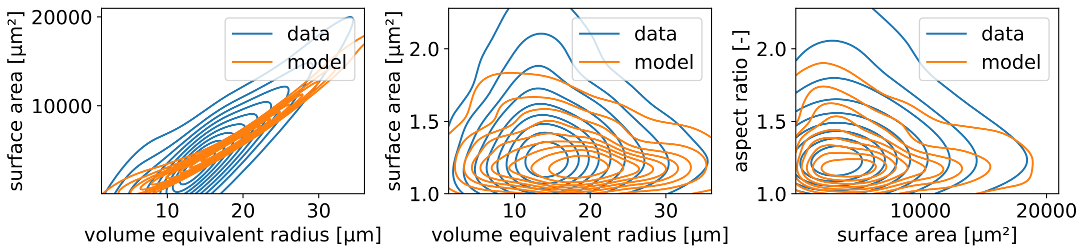

Figure 6: Bivariate (number-weighted) contour plots of geometric descriptors for measured particles and particles drawn from the spherical harmonics model for the CSM-LHT-1 sample. Depicted are volume and surface area (left), volume and aspect ratio (center), and surface area and aspect ratio (right).

3.2 Mesh coarsening

As the high-resolution meshes produced by the spherical harmonics model are not suitable for use in DEM simulations, we compute coarsened meshes as discussed in Section 2.4. Figure 7 shows two exemplary particles and corresponding coarsened meshes obtained by quadric decimation and by the mesh coarsening algorithm described in Section 2.4, using three different loss functions of the form given in Eq. (9).

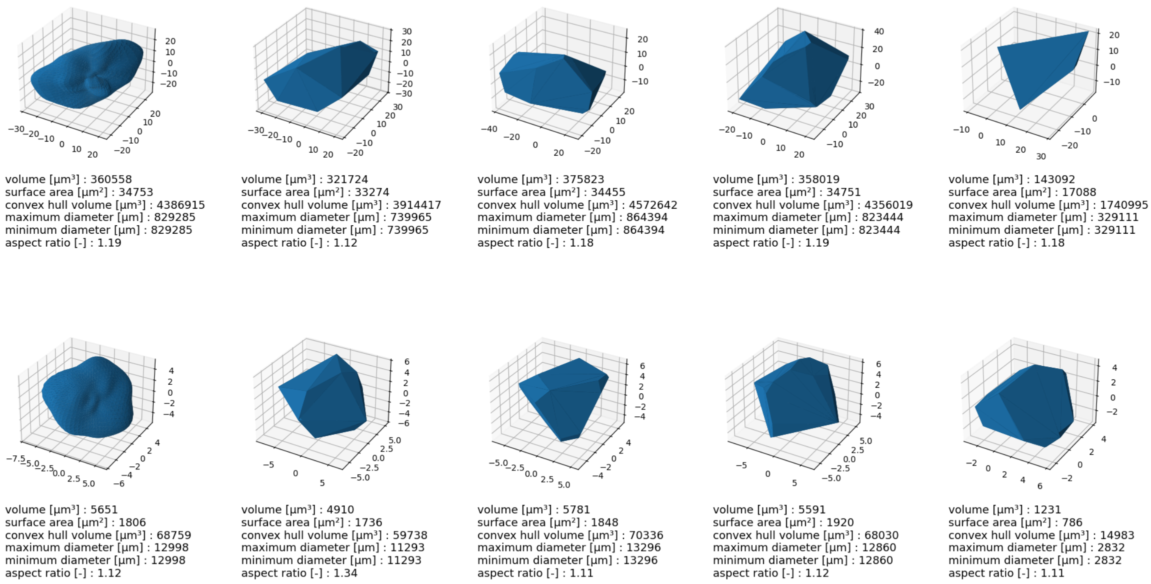

Figure 7: Columns from left to right: 1. Samples of spherical harmonics representations fitted to measured particles. 2. Corresponding coarsened meshes (20 faces) obtained by quadric decimation. 3. Meshes optimized for volume, convex hull volume, max. diameter, min. diameter, surface area and aspect ratio. 4. Meshes optimized for volume, surface area and aspect ratio. 5. Meshes optimized for aspect ratio and intersection-over-union.

Clearly, the choice of geometric descriptors that are included in the loss function heavily influences the resulting coarsened mesh. Since the visual impression is not conclusively informative for goodness-of-fit, we quantify the accuracy by computing each geometric descriptor for the coarsened meshes with $n = 20$ facets using several different loss functions.

We use the values computed based on the fine mesh resulting from the spherical harmonics representation with $l_{\max} = 10$ as a baseline reference.

The resulting RMSREs, as defined in Eq. (10), are shown in Figure 8 and highlight the importance of choosing an appropriate weight function in the mesh optimization method proposed in this paper. Notably, optimizing only for a pixel-wise error given by the IoU (4-th row in Figure 8) yields a poor fit with respect to all considered geometric descriptors. On the other hand, optimizing for all geometric descriptors (ignoring IoU) results in a remarkably good fit, suggesting that this method can be used to optimize for many descriptors simultaneously. Compared to the quadric decimation approach, the optimization with this loss function roughly halves the RMSREs on all geometric descriptors considered.

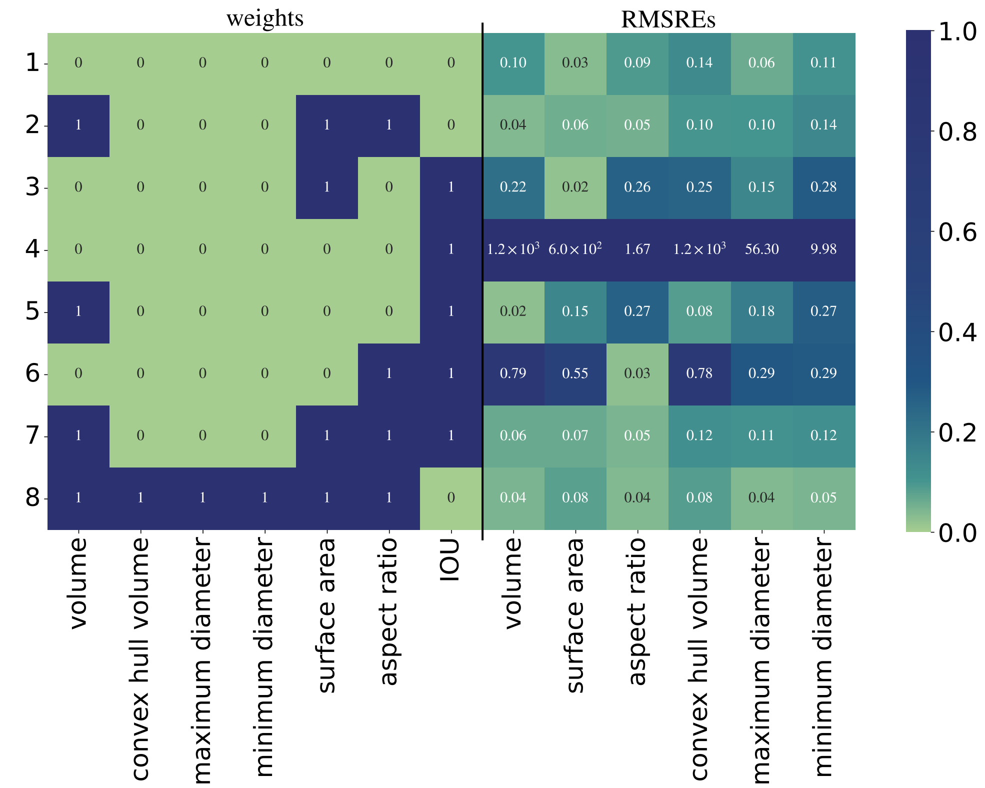

Figure 8: RMSREs for comparing geometric descriptors computed on high-resolution meshes and on meshes obtained by different coarsening strategies. The first row (all weights are set to 0) corresponds to the quadric decimation approach, whereas the other rows correspond to the optimization approach introduced in this paper, using the given weights for the loss function considered in Eq. (9). Based on 150 randomly selected particles from the CSM-LHT-1 sample.

3.3 DEM simulations

For the DEM simulation performed in this study, the mesh coarsening approach stated in Section 2.4 and the data handling principle stated in Section 2.5 were used to generate a total of 378000 particles from a set of $N = 10$ representative particle geometries, each represented as a convex polyhedron with 20 faces. The particle sizes were assigned according to a discrete size distribution that was chosen based on the size distribution observed in the measured image data. A coarse-graining factor of 10 [39] was applied to reduce computational cost while preserving bulk behavior. These parameters are chosen as a compromise between computational efficiency and physical realism and are not calibrated to measurement data from calibration experiments like the static or dynamic angle of repose.

After all particles in the DEM simulation reached a velocity close to zero, the particle positions and radii of the final time step are exported and projected onto the vertical x-z and y-z plane. The surface of the pile is extracted as the upper envelope of the projected particles. The assembly is traversed from the base upwards, and the surface is taken as the top of the connected column of particles, i.e., the uppermost particle before the first vertical gap that exceeds a multiple of the mean particle diameter. Individual particles adhering to the confining geometry above the pile are thereby excluded from the profile, and a rolling median filter is applied to remove residual outliers.

The static angle of repose is then obtained from a linear regression of the surface profile by the method of least squares. Following the approach described in [44], the uppermost 15% and the lowermost 15% of the pile height are excluded from the regression, since the profile is rounded near the apex and flattens out towards the toe; both effects bias the fitted slope towards lower values. The static angle of repose $\alpha = \arctan |m|$ is the angle between the fitted line of slope m and the x-axis.

Two triangle models are evaluated on the surface profile. In the asymmetric model, the left and right flanks are fitted independently; the dividing point is determined as the break point of two piecewise linear regressions, i.e., the position minimizing the summed squared residuals of both lines, and the apex is obtained as their intersection. In the symmetric model, both flanks share a single angle with the apex position varied to minimize the residual.

To ensure sufficient statistical reliability, the evaluation is repeated on two mutually orthogonal vertical sections through the pile, as illustrated in the two images of the static angle of repose. The left image shows the evaluation in the x-z plane, the right image in the y-z plane.

We stress that for the simulations performed in this study, the relevant contact parameters have not yet been calibrated to experimentally measured data. Aside from actual material parameters, this calibration will also adjust for geometric properties of the individual particles which cannot be resolved in the coarsened meshes, e.g., surface roughness, non-convexity or particles on smaller length scales. The determination of final, experimentally validated contact parameters is the subject of a subsequent calibration step, during which the simulation will be adjusted to reflect the actual material behavior.

In future work, the here established workflow provides the methodological basis for further, more realistic DEM simulations of regolith behavior under process- and mission-relevant boundary conditions, thereby laying the groundwork for the systematic modeling of transport, dosing and reaction processes within future ISRU systems, such as the Mini-ROXY lunar demonstrator [8].

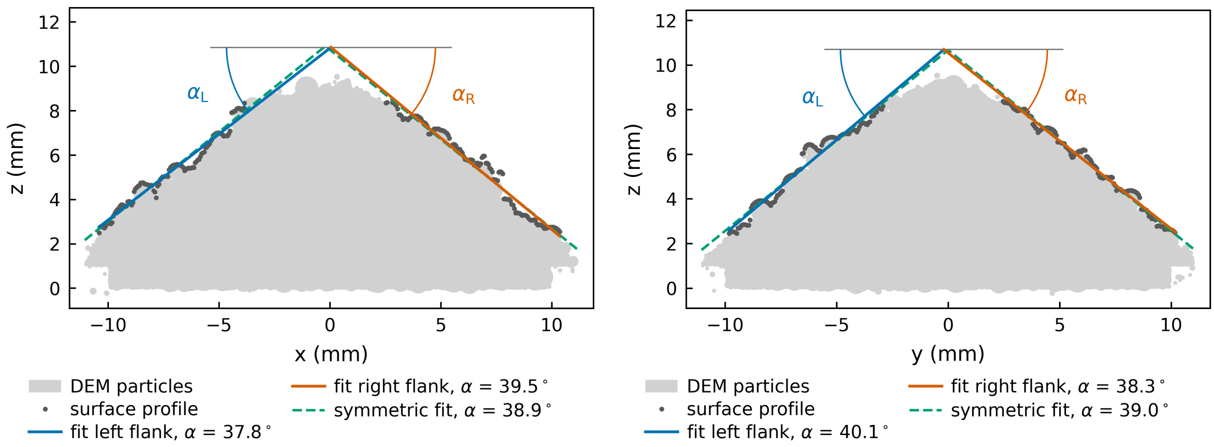

(a) x-z plane

(b) y-z plane

Figure 9: Static angle of repose evaluated in two orthogonal vertical sections. Grey: projected DEM particles. Dark points: extracted surface profile within the regression range. Blue and orange: independent least-squares fits of the left and right flank. Green dashed: symmetric fit with a single shared angle.

4 Conclusion

In this manuscript, we proposed a 3D stochastic model for the geometry of regolith (simulant) particles, contributing to establishing the UPREB knowledge chain for a predictive model of regolith behavior. The model is based on a spherical harmonics expansion and can generate virtual particles that can capture the general shapes of particles. Moreover, we presented a method to obtain coarsened geometries suitable for DEM simulations, retaining key geometric descriptors of the original particles.

The distributions of geometric descriptors for measured particles suggest that multimodality of certain descriptors may exist in some materials. This behavior can occur when the material is a mixture of two or more constituents from different sources. The discussed spherical harmonics model can be extended to a mixture of models in order to capture multi-modal behavior. In future work, application of an (unsupervised) clustering algorithm to the geometric descriptors computed for a large set of individual measured particles can yield insights into the necessary amount of model components. Such a clustering can then also be used to identify an appropriate amount of representative geometries for use in DEM simulations.

The proposed method for mesh coarsening can be tailored to accurately replicate specific geometric descriptors while limiting the number of faces to a specified number. This flexibility can be used to investigate the sensitivity of DEM simulation results with respect to these parameters. However, we have shown that the mesh coarsening is capable of simultaneously replicating a variety of different descriptors and thus, the question of which descriptors should preferably be replicated remains open. Further investigations are also needed to analyze how the number of faces influences the DEM simulation results or the calibrated DEM parameters. Finally, these investigations will enable studies on how the distribution of geometric descriptors influences macroscopic properties (e.g., angle of repose) of a sample. These questions will be considered in future work on calibrating and validating the DEM simulations and on microstructure-property relationships of regolith and regolith simulants.

Acknowledgments

This work was funded by the German Federal Ministry for Research, Technology and Space (BMFTR) within the scope of the National Space Program (Nationales Raumfahrtprogramm), administered by the German Aerospace Center (DLR) under grant number 50EX2667.

References

[1] A. Seidel, M. Altenburg, E. Monchieri, F. Strigl, P. Quadbeck, C. Redlich and U. Pal. ROXY – An economically viable process to produce oxygen and metals from regolith. In T. Leimkuehler and S. Macleod, editors, *Proceedings of the 51st International Conference on Environmental Systems*, 2022. ICES-2022-140.

[2] T. F. Birch, A. Seidel, J. E. Johnson, G. Poehle and U. Pal. Economic analysis of a ROXY pilot plant supporting early lunar mission architectures. *Aerospace*, 13:86, 2026.

[3] K. C. Laurini and W. H. Gerstenmaier. The global exploration roadmap and its significance for NASA. *Space Policy*, 30:149–155, 2014.

[4] G. H. Heiken, D. T. Vaniman and B. M. French, editors. *Lunar Sourcebook: A User's Guide to the Moon*. Cambridge University Press, 1991.

[5] I. Troisi, P. Lunghi and M. Lavagna. Oxygen extraction from lunar dry regolith: Thermodynamic numerical characterization of the carbothermal reduction. *Acta Astronautica*, 199:113–124, 2022.

[6] M. Haeming, A. Seidel and U. Zell. Electrolysis apparatus for the electrolytic production of oxygen from oxide-containing starting material, 2022. U.S. Patent No. 11479869 B2.

[7] A. Seidel, U. B. Pal, P. Quadbeck and A. Adrian. Method and system for extracting metal and oxygen from powdered metal oxides, 2021. U.S. Patent No. 20230131891 A1.

[8] A. Seidel, E. Monchieri, M. Altenburg, M. Franz, T. Birch, G. Pöhle, C. Redlich and U. Pal. Oxygen from regolith: The Mini-ROXY lunar demonstration instrument and mission. In *Proceedings of the 54th International Conference on Environmental Systems*, 2025. ICES-2025-107.

[9] A. Chiaramonti and E. Garboczi. 3D shape and size data for 10084 and 14163 lunar regolith particles, 2024. `https://doi.org/10.18434/mds2-3043`. Accessed 2026-06-30.

[10] H. Wu, Y. Zou, C. Zhang, W. Yang, B. Wu, K. Yung and Q. Zhao. Micro-CT characterization of the Chang'e-5 lunar regolith samples. *Journal of Geophysical Research: Planets*, 130:e2024JE008787, 2025.

[11] H. R. Norouzi, R. Zarghami, R. Sotudeh-Gharebagh and N. Mostoufi. *Coupled CFD-DEM Modeling: Formulation, Implementation and Application to Multiphase Flows*. John Wiley & Sons, 1st edition, 2016.

[12] Z. Y. Zhou, S. B. Kuang, K. W. Chu and A. B. Yu. Discrete particle simulation of particle–fluid flow: model formulations and their applicability. *Journal of Fluid Mechanics*, 661:482–510, 2010.

[13] C. Coetzee. Review: Calibration of the discrete element method. *Powder Technology*, 310:104–142, 2017.

[14] O. C. Scheffler and C. Coetzee. DEM calibration for simulating bulk cohesive materials. *Computers and Geotechnics*, 161:105476, 2023.

[15] K. Dong, C. Wang and A. Yu. A novel method based on orientation discretization for discrete element modeling of non-spherical particles. *Chemical Engineering Science*, 126:500–516, 2015.

[16] C. Xie, T. Song and Y. Zhao. Discrete element modeling and simulation of non-spherical particles using polyhedrons and super-ellipsoids. *Powder Technology*, 368:253–267, 2020.

[17] P. Cundall. Formulation of a three-dimensional distinct element model—Part I. A scheme to detect and represent contacts in a system composed of many polyhedral blocks. *International Journal of Rock Mechanics and Mining Sciences & Geomechanics Abstracts*, 25:107–116, 1988.

[18] R. Hart, P. Cundall and J. Lemos. Formulation of a three-dimensional distinct element model—Part II. Mechanical calculations for motion and interaction of a system composed of many polyhedral blocks. *International Journal of Rock Mechanics and Mining Sciences & Geomechanics Abstracts*, 25:117–125, 1988.

[19] A. Mittal, N. Mangadoddy and R. Banerjee. GPU based discrete element modeling for convex polyhedral shape particles: Development and validation. *Powder Technology*, 449:120407, 2025.

[20] S. N. Chiu, D. Stoyan, W. S. Kendall and J. Mecke. *Stochastic Geometry and Its Applications*. John Wiley & Sons, 3rd edition, 2013.

[21] P. J. M. Van Laarhoven and E. H. L. Aarts. *Simulated Annealing: Theory and Applications*. Springer, 1987.

[22] T. Birch, A. Seidel, E. Monchieri, M. Franz, M. Altenburg, M. Weber, V. Schmidt, O. Furat, U. Peuker, R. Ditscherlein, L. Ditscherlein, C. Schilde, T. Lamping, G. Pöhle and C. Redlich. UPREB: Universal Predictors of Regolith Behaviour – Concept and Overview. In *54th International Conference on Environmental Systems*. International Conference on Environmental Systems, 2025.

[23] M. Weber, R. Ditscherlein, L. Ditscherlein, T. Birch, M. Franz, A. Seidel, U. A. Peuker, O. Furat, V. Schmidt and G. Pöhle. Statistical analysis and modeling of the 3D morphology and texture of lunar regolith simulants. *Microscopy and Microanalysis*, 32:ozag013, 2026.

[24] R. Ditscherlein, T. Leißner and U. A. Peuker. Preparation strategy for statistically significant micrometer–sized particle systems suitable for correlative 3D imaging workflows on the example of X–ray microtomography. *Powder Technol.*, 395: 235–242, 2022.

[25] S. Berg, D. Kutra, T. Kroeger, C. N. Straehle, B. X. Kausler, C. Haubold, M. Schiegg, J. Ales, T. Beier, M. Rudy, K. Eren, J. I. Cervantes, B. Xu, F. Beuttenmueller, A. Wolny, C. Zhang, U. Koethe, F. A. Hamprecht and A. Kreshuk. ilastik: interactive machine learning for (bio)image analysis. *Nat. Methods*, 16:1226–1232, 2019.

[26] H. Wadell. Sphericity and Roundness of Rock Particles. *The Journal of Geology*, 41: 310–331, 1933.

[27] M. Dawson-Haggerty et al. trimesh, 2026. URL `https://trimesh.org`. Accessed 2026-03-02.

[28] E. Hobson. *The Theory of Spherical and Ellipsoidal Harmonics*. Cambridge University Press, 2012.

[29] J. Feinauer, A. Spettl, I. Manke, S. Strege, A. Kwade, A. Pott and V. Schmidt. Structural characterization of particle systems using spherical harmonics. *Materials Characterization*, 106:123–133, 2015.

[30] D. Marinucci and G. Peccati. *Random Fields on the Sphere: Representation, Limit Theorems and Cosmological Applications*. Cambridge University Press, 2011.

[31] A. Lang and C. Schwab. Isotropic Gaussian random fields on the sphere: Regularity, fast simulation and stochastic partial differential equations. *The Annals of Applied Probability*, 25:3047–3094, 2015.

[32] M. A. Wieczorek and M. Meschede. SHTools: Tools for working with spherical harmonics. *Geochemistry, Geophysics, Geosystems*, 19:2574–2592, 2018.

[33] J. Zhao, S. Zhao and S. Luding. The role of particle shape in computational modelling of granular matter. *Nature Reviews Physics*, 5:505–525, 2023.

[34] D. Höhner, S. Wirtz and V. Scherer. A study on the influence of particle shape on the mechanical interactions of granular media in a hopper using the Discrete Element Method. *Powder Technology*, 278:286–305, 2015.

[35] M. Garland and P. S. Heckbert. Surface simplification using quadric error metrics. In *Proceedings of the 24th annual conference on Computer graphics and interactive techniques - SIGGRAPH '97*, pages 209–216. ACM Press, 1997.

[36] D. Cohen-Steiner, P. Alliez and M. Desbrun. Variational shape approximation. *ACM Transactions on Graphics*, 23:905–914, 2004.

[37] W. J. Schroeder, J. A. Zarge and W. E. Lorensen. Decimation of triangle meshes. *ACM SIGGRAPH Computer Graphics*, 26:65–70, 1992.

[38] S. Forstmann. Fast-Quadric-Mesh-Simplification. GitHub repository, 2014. URL `https://github.com/sp4cerat/Fast-Quadric-Mesh-Simplification`. Accessed: 2026-07-07.

[39] Z. Zhou, G. Jin, Y. Liu, C. Gao, H. Ma, S. Bai and J. Song. A coarse-grained CFD-DEM method for efficient simulation of fluid-solid coupling failure process in geomaterials: methodology and verification. *Powder Technology*, 467:121483, 2026.

[40] H. Hertz. Über die Berührung fester elastischer Körper. *Journal für die reine und angewandte Mathematik*, 92:156–171, 1881.

[41] R. D. Mindlin and H. Deresiewicz. Elastic spheres in contact under varying oblique forces. *Journal of Applied Mechanics*, 20:327–344, 1953.

[42] K. L. Johnson, K. Kendall and A. D. Roberts. Surface energy and the contact of elastic solids. *Proceedings of the Royal Society of London. A. Mathematical and Physical Sciences*, 324:301–313, 1971.

[43] O. Furat, T. Leißner, K. Bachmann, J. Gutzmer, U. A. Peuker and V. Schmidt. Stochastic modeling of multidimensional particle properties using parametric copulas. *Microscopy and Microanalysis*, 25:720–734, 2019.

[44] C. Sunday, N. Murdoch, S. Tardivel, S. R. Schwartz and P. Michel. Validating N-body code chrono for granular DEM simulations in reduced-gravity environments. *Monthly Notices of the Royal Astronomical Society*, 498:1062–1079, 2020.